

# PPISP: Physically-Plausible Compensation and Control of Photometric Variations in Radiance Field Reconstruction

Isaac Deutsch,\* Nicolas Moënne-Locoz,\* Gavriel State, Zan Gojcic

NVIDIA

{ideutsch, nicolasm, gstate, zgojcic}@nvidia.com

<https://research.nvidia.com/labs/sil/projects/ppisp/>



Figure 1. We introduce a differentiable image processing pipeline applied to radiance field reconstruction. By modeling the behavior of conventional cameras, our approach disentangles image formation effects from the rest of the pipeline. Our physically-plausible model admits a controller module that predicts exposure and color changes for novel views.

## Abstract

*Multi-view 3D reconstruction methods remain highly sensitive to photometric inconsistencies arising from camera optical characteristics and variations in image signal processing (ISP). Existing mitigation strategies such as per-frame latent variables or affine color corrections lack physical grounding and generalize poorly to novel views. We propose the Physically-Plausible ISP (PPISP) correction module, which disentangles camera-intrinsic and capture-dependent effects through physically based and interpretable transformations. A dedicated PPISP controller, trained on the input views, predicts ISP parameters for novel viewpoints, analogous to auto exposure and auto white balance in real cameras. This design enables realistic and fair evaluation on novel views without access to ground-truth images. PPISP achieves SoTA performance on standard benchmarks, while providing intuitive control and supporting the integration of metadata when available. The source code is available at: <https://github.com/nv-tlabs/ppisp>*

## 1. Introduction

State-of-the-art multi-view 3D reconstruction methods have significantly advanced the fidelity of novel view synthesis (NVS), transforming it into a technology with real-world applications in physical AI simulation, virtual production, and content creation. Despite these advances, the quality of reconstruction and view synthesis remains highly sensitive to the quality of the input data—both to the distribution of camera poses and to multi-view appearance inconsistencies. The latter often arise from variations in camera optical characteristics and image signal processing (ISP) settings over time. These variations result in differences in color tone, intensity, and contrast that violate the photometric consistency assumptions underlying 3D reconstruction.

A common strategy to mitigate these appearance variations is to introduce additional, optimizable per-frame or per-camera parameters designed to capture photometric residuals while preserving a consistent multi-view scene representation. Recent state-of-the-art approaches include low-dimensional generative latent optimization (GLO) vectors [15], learnable affine transformations [21], and bilateral grids (BilaRF) [28]. However, these mitigation strategies face several trade-offs and challenges:

\* Equal contribution.

- **Representation capacity:** higher-capacity and less-constrained modules tend to improve PSNR on the training views but risk modeling more than just photometric variations, often degrading NVS quality.
- **Interpretability and controllability:** the learned parameters are typically non-interpretable (*e.g.*, in GLO or BiLaRF), making it difficult to intuitively adjust properties such as brightness or white balance.
- **Parameters for novel views:** since the parameters are optimized independently per frame, it is unclear how to assign appropriate values when synthesizing novel views.

The latter is especially challenging due the tendency of these modules to conflate camera sensor intrinsic properties (*e.g.*, vignetting and camera response function) with capture-dependent settings that vary per frame or are adjusted by the ISP (*e.g.*, exposure time and white balance). As a consequence, evaluation protocols commonly assume access to the ground-truth novel view image and estimate a corrective mapping, such as an affine transform, quadratic polynomial, or direct parameter optimization, to minimize the difference between the synthesized and the ground-truth (GT) image before computing the evaluation metrics. But such protocols are inherently flawed as they: **(i)** deviate from real-world scenarios where GT novel views are unavailable, and **(ii)** conceal differences between methods by compensating for them through the corrective mapping.

To address these challenges, we propose a Physically-Plausible ISP (PPISP) correction module, grounded in the physical principles of camera image formation. Specifically, we disentangle sensor-intrinsic properties and capture-dependent settings through dedicated per-sensor and per-frame modules, respectively, and constrain their effects according to the image formation process (*e.g.*, the exposure module can only modify the overall image brightness). Our model acts as a post-processing step applied to the raw images rendered from the 3D representation, and enables direct controllability through manual change of the parameters. Moreover, we introduce a PPISP controller that predicts the parameters of the per-frame modules for novel views, analogous to the auto exposure and auto white balance mechanisms in conventional cameras.

## 2. Related Work

Appearance inconsistencies across multi-view input images significantly degrade the quality of radiance field reconstructions and subsequent novel-view synthesis. Such variations are common in unconstrained image collections, for instance when using internet photo collections or captures under uncontrolled lighting conditions.

**Compensation during reconstruction.** To mitigate these inconsistencies, NeRF-W [15] and GS-W [31] introduce

learnable per-image latent embeddings (GLO) that are optimized jointly with the scene representation. These latent embeddings enable smooth interpolation within the observed appearance distribution, but may inadvertently get entangled with scene geometry or reflectance when optimized end-to-end. To impose stronger constraints and better align with the image formation process, subsequent works model photometric transformations explicitly. URF [21] represents per-image variations using affine color transformations, while BiLaRF [28] extends this idea to per-pixel affine mappings parameterized via bilateral grids. Closest to our approach, ADOP’s [22] post-processing models exposure, white balance, camera response function (CRF), and vignetting effects as explicit calibration parameters. However, our formulation better disentangles exposure offset and white balance, while using a more compact CRF model. Recently, Huang *et al.* [11] and Niemeyer *et al.* [17] deviate from a frame-based correction and instead learn a 3D exposure neural field, predicting the optimal exposure values for each 3D point.

**Harmonizing appearance during preprocessing.** An alternative strategy is to decouple the compensation from reconstruction and harmonize the input images as a preprocessing step. Shin *et al.* [24] employ a transformer network to predict bilateral grids that harmonize each image to a chosen reference view. Alzayer *et al.* [1] instead use a diffusion model to relight images directly, but due to the lack of paired real data, they train their generative model only on synthetic data. To overcome this limitation, Trevithick *et al.* [27] propose a data generation pipeline that starts from harmonized multi-view inputs and employs a generative model to augment them with diverse lighting conditions. The resulting pseudo-paired dataset enables supervised training of harmonization networks using the original, appearance-consistent images as ground-truth.

**Novel view synthesis with target appearance.** The above methods reconstruct the scene in a canonical or reference appearance, but it remains unclear how to set the parameters of their appearance modules to render an image in a desired target appearance. This target appearance could be user defined or selected to match the appearance that a camera with auto exposure and white balance would produce. This ambiguity poses practical challenges for novel view synthesis and complicates fair evaluation under photometric variation. Prior work typically applies post-render normalization that assumes access to the target image during evaluation: NeRF-W [15] fine-tunes latent embeddings on one half of each image and evaluates on the other, RawNeRF [16] performs channel-wise affine alignment, Mip-NeRF 360 [2] uses a quadratic color basis alignment, and ADOP [22] re-optimizes per-frame parameters.

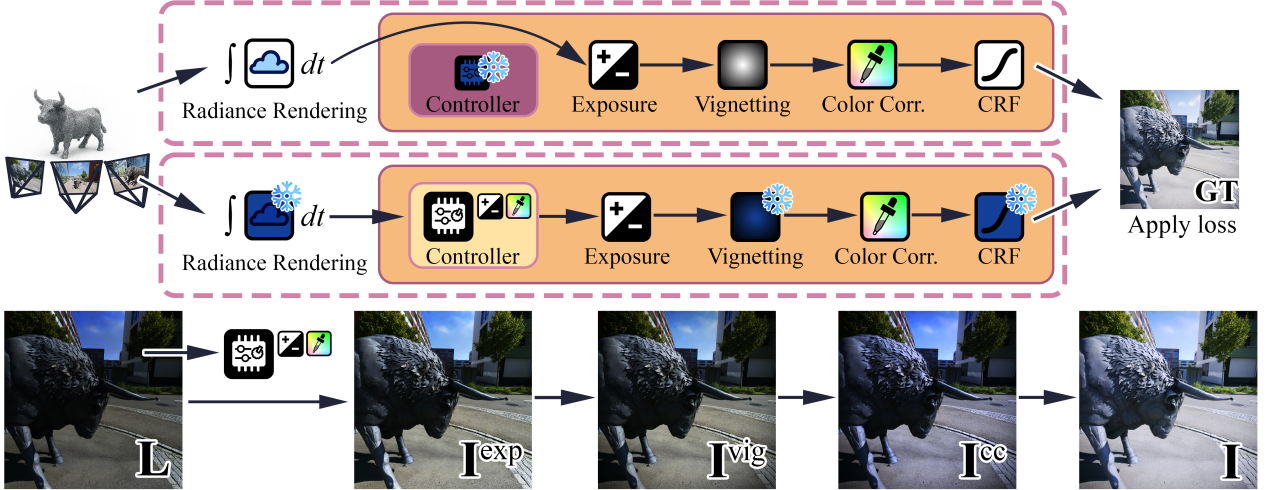


Figure 2. Our proposed pipeline applies a sequence of physically-grounded modules to the input reconstructed radiance (exposure offset, chromatic vignetting, linear color correction and non-linear camera response function). Top: all modules except the controller are jointly optimized during the first training phase. Bottom: the controller is then trained to predict per-frame exposure and color correction for novel views while other modules are frozen. The image sequence shows intermediate outputs after each successive module is applied, illustrating the progressive effects of the pipeline.

Such evaluation protocols, however, (i) mask differences between methods and (ii) are infeasible in real-world applications where access to the target image cannot be assumed. In line with the principle that novel views should be rendered solely from reconstructed data without access to target pixels, we introduce a PPISP controller that takes the *raw* radiance image rendered from the 3D representation as input and outputs the PPISP parameters. We optimize this network on the training views and then directly apply it to the novel views during inference. Somewhat related to our PPISP controller, [18, 26] train a network to predict exposure control for improved feature matching and object detection, respectively.

### 3. Preliminaries

**Radiance Field Reconstruction** aims to optimize a parametric representation of a scene’s volumetric density  $\sigma \in \mathbb{R}$  and emitted radiance  $\mathbf{c} \in \mathbb{R}^3$ . The radiance  $\mathbf{L}(\mathbf{r})$  of a camera ray  $\mathbf{r}(x) = \mathbf{o} + x \mathbf{d}$  with origin  $\mathbf{o} \in \mathbb{R}^3$  and direction  $\mathbf{d} \in \mathbb{R}^3$  is rendered from this representation as

$$\mathbf{L}(\mathbf{r}) = \int_{near}^{far} T(x) \sigma(\mathbf{r}(x)) \mathbf{c}(\mathbf{r}(x)) dt, \quad (1)$$

where  $T(x) = \exp(-\int_{near}^x \sigma(\mathbf{r}(y)) dy)$  denotes the transmittance along the ray. The optimization is supervised using ground truth images  $\mathbf{I}$  captured by one or more cameras with known extrinsics and intrinsics. This standard formulation alone does not account for camera-specific imaging effects.

**Camera Image Formation** is the process through which the radiance  $\mathbf{L}$  is converted to the final image:

$$\mathbf{I} = \mathcal{F}(\mathbf{L}; \Theta), \quad (2)$$

Here, the function  $\mathcal{F}(\cdot)$  models the complete image acquisition process, including lens distortions (e.g., vignetting, chromatic aberrations), exposure settings (aperture, shutter time), sensor characteristics (spectral response, noise, gain), and ISP operations according to some parameters  $\Theta$ . While some components of this process remain constant across acquisition time, others may vary due to manual adjustments or automatic adaptation by the sensor controller.

**Notation.** Let  $\mathbf{I} \in \mathbb{R}^{H \times W \times 3}$  be an RGB image. The color at spatial location  $\mathbf{u} = (i, j)$  is  $\mathbf{x} = \mathbf{I}_{i,j} \in \mathbb{R}^3$  and its  $k$ -th channel value is  $x = \mathbf{x}_k = \mathbf{I}_{i,j,k} \in \mathbb{R}$ ,  $k \in \{R, G, B\}$ . Operations defined on channel values or colors are understood element-wise when applied to an image.

### 4. Method

We compensate for photometric inconsistencies across input images by jointly optimizing the scene representation together with a differentiable ISP pipeline that approximates the camera image formation function  $\mathcal{F}(\cdot)$  defined in Eq. (2). During optimization, this pipeline models both camera-specific and time-varying effects. During inference (*i.e.*, when rendering novel views), the learned controller (Sec. 4.5) predicts the time-varying parameters directly from the radiance  $\mathbf{L}$  rendered from the scene representation.

Our ISP pipeline consists of four sequential modules (see Fig. 2):

- *Exposure offset* accounts for aperture, shutter time and gain variations,
- *Vignetting* models optical attenuation across the sensor,
- *Color correction* models sensor spectral response and white balance adjustments,
- *Camera response function* (CRF) applies a non-linear transformation from sensor irradiance to image colors.

Following [8], the first three modules operate linearly on the scene radiance, while the CRF provides the final non-linear mapping. Fig. 2 shows an overview of the pipeline in the context of the radiance reconstruction and illustrates the individual parts and their effects.

#### 4.1. Exposure Offset

We model exposure as a global, per-frame scale on the radiance using a base-2 exponent, mimicking photographic exposure values:

$$\mathbf{I}^{\text{exp}} = \mathcal{E}(\mathbf{L}; \Delta t) = \mathbf{L} 2^{\Delta t}, \quad (3)$$

where  $\Delta t \in \mathbb{R}$  is an optimizable exposure offset. This offset represents the variation of the radiance intensity reaching the sensor and is specific to the capture. Thus, we estimate one such offset for each frame.

#### 4.2. Vignetting

Following Goldman [7], we model per-channel radial intensity falloff using a polynomial in the squared radius around an optimizable optical center:

$$\mathbf{I}^{\text{vign}} = \mathcal{V}(\mathbf{I}^{\text{exp}}; \boldsymbol{\mu}, \boldsymbol{\alpha}) = \mathbf{I}^{\text{exp}} \cdot v(r; \boldsymbol{\alpha}), \quad (4)$$

where  $\boldsymbol{\mu} \in \mathbb{R}^2$  is the optical center,  $\boldsymbol{\alpha} \in \mathbb{R}^3$  are polynomial coefficients, and  $r = \|\mathbf{u} - \boldsymbol{\mu}\|_2$  is the distance of the pixel location  $\mathbf{u}$  to the optical center. The attenuation factor  $v(r)$  is defined as:

$$v(r) = \text{clip}_{(0,1)}(1 + \alpha_1 r^2 + \alpha_2 r^4 + \alpha_3 r^6). \quad (5)$$

At the start of optimization, we initialize  $\boldsymbol{\alpha} = 0$  and let  $\boldsymbol{\mu}$  be the image center.

Since our vignetting model is chromatic, a falloff polynomial is defined for each color channel by distinct parameter values.

#### 4.3. Color Correction

To model effects such as white balance, which may vary per-frame, and gamut differences between multiple cameras, we apply color correction. To disentangle it from exposure correction, we apply a  $3 \times 3$  homography  $\mathbf{H}$  on RG chromaticities and intensity — following Finlayson *et al.* [6] — and ensure normalization of the intensity after the

transform. Inspired by DeTone *et al.* [4], we parameterize the color correction as four chromaticity offsets  $\Delta \mathbf{c}_k$ , construct  $\mathbf{H}$  from them, and apply the color correction:

$$\mathbf{I}^{\text{cc}} = \mathcal{C}(\mathbf{I}^{\text{vign}}, \{\Delta \mathbf{c}_k\}_{k \in \{R,G,B,W\}}) = h(\mathbf{I}^{\text{vign}}; \mathbf{H}). \quad (6)$$

Let  $\mathbf{C} \in \mathbb{R}^{3 \times 3}$  denote the RGB→RGI conversion matrix and  $\mathbf{C}^{-1}$  its inverse. The intensity normalization can then be defined as :

$$n(\mathbf{x}; \mathbf{H}) \doteq \frac{\mathbf{x}_R + \mathbf{x}_G + \mathbf{x}_B}{[\mathbf{H} \cdot \mathbf{C} \mathbf{x}]_3 + \varepsilon}. \quad (7)$$

Here,  $\varepsilon$  is a small constant for numerical stability. This normalization decouples exposure from chromatic correction. The color transform follows compactly as

$$h(\mathbf{x}; \mathbf{H}) \doteq \mathbf{C}^{-1}(n(\mathbf{x}; \mathbf{H}) \cdot (\mathbf{H} \cdot \mathbf{C} \mathbf{x})). \quad (8)$$

To construct  $\mathbf{H}$ , we define four 2D source–target chromaticity pairs. Specifically, we fix the source RG chromaticities  $\mathbf{c}_{s, \cdot}$  to the three primaries and a neutral white:

$$\begin{aligned} \mathbf{c}_{s,R} &= (1, 0)^T; & \mathbf{c}_{s,G} &= (0, 1)^T; \\ \mathbf{c}_{s,B} &= (0, 0)^T; & \mathbf{c}_{s,W} &= \left(\frac{1}{3}, \frac{1}{3}\right)^T, \end{aligned} \quad (9)$$

and define the targets  $\mathbf{c}_{t, \cdot}$  as offsets from these sources  $\mathbf{c}_{t,k} = \mathbf{c}_{s,k} + \Delta \mathbf{c}_k$  for  $k \in \{R, G, B, W\}$ . By lifting the 2D chromaticities to homogeneous coordinates and stacking them as  $\mathbf{S} \doteq [\tilde{\mathbf{c}}_{s,R} \ \tilde{\mathbf{c}}_{s,G} \ \tilde{\mathbf{c}}_{s,B}]$  and  $\mathbf{T} \doteq [\tilde{\mathbf{c}}_{t,R} \ \tilde{\mathbf{c}}_{t,G} \ \tilde{\mathbf{c}}_{t,B}]$ , we can define

$$\mathbf{M} \doteq [\tilde{\mathbf{c}}_{t,W}] \times \mathbf{T}, \quad (10)$$

where  $[\cdot] \times$  is the skew-symmetric cross-product matrix. Then,  $\mathbf{k} \in \mathbb{R}^3$  can be obtained via a cross-product of any pair of linearly independent rows  $i$  and  $j$ ,

$$\mathbf{k} \propto \mathbf{m}_i \times \mathbf{m}_j. \quad (11)$$

where  $\mathbf{m}_1, \mathbf{m}_2, \mathbf{m}_3$  are the rows of  $\mathbf{M}$ . Finally, we form and normalize

$$\mathbf{H} = \mathbf{T} \text{diag}(\mathbf{k}) \mathbf{S}^{-1}, \quad \mathbf{H} \leftarrow \frac{\mathbf{H}}{[\mathbf{H}]_{3,3}}. \quad (12)$$

A precise derivation and further details are provided in the Supplementary.

#### 4.4. Camera Response Function

Inspired by Grossberg and Nayar [9], we use a piecewise power curve to model non-linear chromatic transformations. The CRF operator  $\mathcal{G}$  has four learned parameters:

$$\mathbf{I} = \mathcal{G}(\mathbf{I}^{\text{cc}}; \tau, \eta, \xi, \gamma). \quad (13)$$

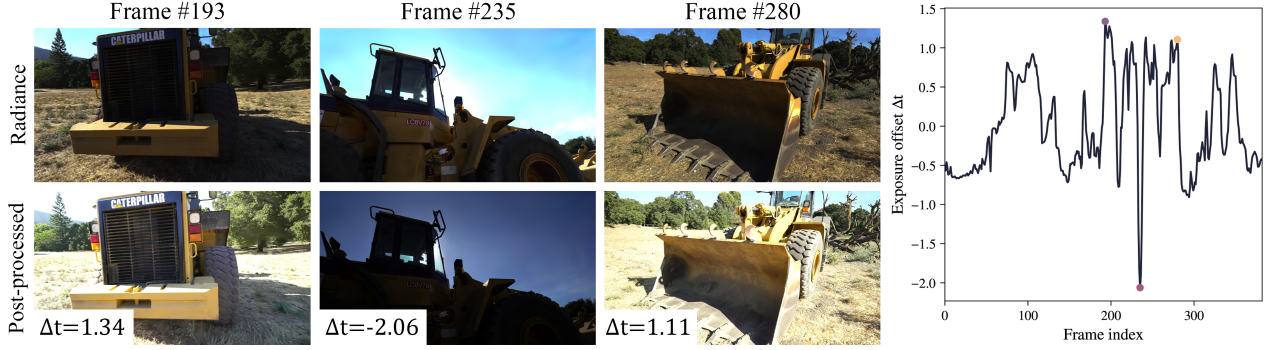


Figure 3. Dynamics of the controller module. The predicted exposure offset (inset) depends on the image content of the rendered radiance. Right side: Plot of exposure offsets as predicted for each frame of the *caterpillar* sequence, with the three displayed frames highlighted.

For each channel, the basic S-shaped curve is given by:

$$f_0(x; \tau, \eta, \xi) = \begin{cases} a \left( \frac{x}{\xi} \right)^\tau, & 0 \leq x \leq \xi, \\ 1 - b \left( \frac{1-x}{1-\xi} \right)^\eta, & \xi < x \leq 1, \end{cases} \quad (14)$$

setting  $a$  and  $b$  to match the slope at the inflection point to ensure  $C^1$  continuity:

$$a = \frac{\eta \xi}{\tau(1-\xi) + \eta \xi}, \quad b = 1 - a. \quad (15)$$

Finally, the CRF image operator  $\mathcal{G}$  is a composition of this S-curve with a gamma correction:

$$\mathcal{G}(x; \tau, \eta, \xi, \gamma) = [f_0(x; \tau, \eta, \xi)]^\gamma. \quad (16)$$

#### 4.5. Per-Frame ISP Parameter Controller

The exposure offsets and color correction transforms introduced above are valid only for a specific capture, *i.e.*, a single camera pose, and therefore cannot be directly reused for novel view rendering. To address this limitation, we introduce a controller that predicts these parameters from the rendered scene radiance, analogous to how auto exposure and auto white balance works in conventional cameras:

$$(\Delta t, \{\Delta \mathbf{c}_k\}_{k \in \{R, G, B, W\}}) = \mathcal{T}(\mathbf{L}). \quad (17)$$

Here,  $\mathcal{T}(\cdot)$  is the camera-specific controller parametric function, which we design as a coarse feature extractor ( $1 \times 1$  convolutions with pooling to a  $5 \times 5$  grid), followed by a parameter regressor (an MLP with separate output heads). The detailed architecture of the controller is provided in the Supplementary.

We optimize the controller in a separate stage once the optimization of the scene representation is complete. At that stage, the underlying reconstruction and all per-camera

ISP parameters are frozen, the controller-predicted parameters are applied through the ISP, and the controller itself is trained using the same photometric loss as in the initial phase. A qualitative example of the controller’s effects is given in Fig. 3. Optional scalar controls (*e.g.*, exposure compensation or EXIF-derived biases) can be concatenated to the regressor input.

#### 4.6. Regularization

Joint optimization of the modules can introduce brightness and color ambiguities between scene radiance and the ISP parameters. To mitigate this, we apply regularization on the previously defined parameters, using the Huber loss  $\mathcal{L}_\delta$ , where  $\delta$  denotes the threshold. We use superscripts to indicate parameters belonging to specific camera sensors<sup>(s)</sup> and frames<sup>(f)</sup>.

**Brightness.** We penalize the mean exposure offset over frames:

$$\mathcal{L}_b = \lambda_b \mathcal{L}_{\delta=0.1} \left( \frac{1}{F} \sum_{f=1}^F \Delta t^{(f)} \right). \quad (18)$$

**Color.** We penalize the frame-mean of the target chromaticity offsets (element-wise in  $\mathbb{R}^2$ ):

$$\mathcal{L}_c = \lambda_c \sum_{k \in \{R, G, B, W\}} \mathcal{L}_{\delta=0.005} \left( \frac{1}{F} \sum_{f=1}^F \Delta \mathbf{c}_k^{(f)} \right). \quad (19)$$

Because chromatic corrections, as done in vignetting and CRF modules, may also introduce localized color shifts, we shrink parameter variance across channels. Let  $\theta_{m,k}$  be the parameters of channel  $k$  for module  $m \in \{\text{vig, crf}\}$ . We penalize their across-channel variance, averaged over parameters:

$$\mathcal{L}_{\text{var}} = \lambda_{\text{var}} \sum_{m \in \{\text{vig, crf}\}} \text{Var}_k(\theta_{m,k}). \quad (20)$$



Figure 4. Qualitative comparison of novel view synthesis. Row labels indicate datasets and sequences (in italics). Column labels indicate methods. Our method achieves more consistent photometry and better color reproduction across various datasets and sequences. Bottom row: When image metadata such as relative exposure is available, our method can incorporate it to produce a more accurate novel view.

**Physically-plausible vignetting.** For each polynomial, we penalize the center and softly enforce  $\alpha_j \leq 0$ :

$$\mathcal{L}_{\text{vig}} = \lambda_v \left( \|\boldsymbol{\mu}_k\|_2^2 + \sum_j [\alpha_j]_+^2 \right). \quad (21)$$

Here  $[x]_+ = \max(x, 0)$  is the elementwise rectifier. The overall regularizer is

$$\mathcal{L}_{\text{reg}} = \mathcal{L}_b + \mathcal{L}_c + \mathcal{L}_{\text{var}} + \mathcal{L}_{\text{vig}}. \quad (22)$$

## 5. Experiments

We begin by evaluating the proposed PPISP correction module and controller on standard novel-view synthesis benchmarks, assessing both reconstruction fidelity and novel-view quality (Sec. 5.1). We then demonstrate how our formulation allows us to incorporate image metadata, such as relative exposure, when available (Sec. 5.2). We measure the runtime performance impact (Sec. 5.3). Finally, we analyze the relationship between model capacity, overfitting behavior, and novel-view synthesis performance (Sec. 5.4).

**Setting.** Since the PPISP module as a post-processing operator is reconstruction-agnostic, we integrate it both in 3DGUT [29] and GSplat [30] (an accelerated implementation of 3DGS [12]).

Comparison baselines are the post-processing approaches described in BilaRF [28] and ADOP [22]. For experiments, we rely on their reference hyperparameters and reference implementations adapted for 3DGUT and GSplat. To increase the stability of ADOP’s method, we increase the strength of their CRF regularization about  $100\times$  compared to the reference value.

We jointly train the reconstruction method (with the default MCMC configuration) and the post-processing operator for 30k iterations. For the PPISP controller, we freeze both and train the controller for an additional 5k iterations.

**Metrics.** We evaluate the perceptual quality of the rendered views using peak signal-to-noise ratio (PSNR), structural similarity (SSIM), and learned perceptual image patch similarity (LPIPS) metrics.

As metrics such as PSNR are highly sensitive to global brightness shifts, and our baselines do not support appearance compensation for novel views, we additionally report metrics computed after affine color alignment, following RawNeRF [16]. We denote this aligned metrics with the suffix “-CC”, but emphasize that such comparison masks the differences between the methods and assumes access to the GT target views, which are not available in practice.

**Datasets.** To show the robustness and generality of our method, we conducted experiments on a variety of publicly

available datasets: Mip-NeRF 360 [2], Tanks and Temples [14], BilaRF [28], HDR-NeRF [10], and nine static sequences of the Waymo Open Dataset [25]. More details about the scenes, resolution, and training-test splits are available in the Supplementary.

To further highlight the differences of the methods in challenging real-world scenarios, we captured a new *PPISP dataset* consisting of four scenes. Each of them was captured with three different cameras (Apple iPhone 13 Pro, Nikon Z7, and OM System OM-1 Mark II) to ensure variations. Further details of this dataset are available in the Supplementary.

### 5.1. Novel View Synthesis Benchmark

Quantitative results on the standard benchmark scenes are presented in Tab. 1, and qualitative comparisons are shown in Fig. 4. Our method consistently outperforms all baselines across all datasets in terms of PSNR, and for most scenes also in terms of SSIM and LPIPS. Notably, it even surpasses the BilaRF baseline [28] when that baseline is given privileged access to the target image, i.e., when comparing our PSNR against the baseline’s PSNR-CC. The relative improvements carry over to the 3DGS [12, 30] integration.

The comparison between PSNR and PSNR-CC further highlights the effectiveness of our controller in reproducing the camera’s auto-exposure and white-balance behavior. On most datasets, the controller achieves metrics close to those obtained after affine color alignment, indicating that it faithfully predicts the necessary per-frame appearance corrections. The only notable discrepancy appears on the BilaRF dataset, likely due to the fact that this dataset contains some manual settings overrides (indicated by the metadata), which are not captured by our controller.

Both PPISP and ADOP [22] employ camera-specific components (vignetting and CRF), which generalize to novel views, leading to improved metrics over BilaRF [28]. Our base image formation model (*w/o ctrl.*) outperforms both baselines thanks to better separation of concerns of the individual modules and stronger constraints (see also Sec. 5.4). We elaborate on a direct comparison to ADOP in the Supplementary. Our base model still falls short of our full pipeline, which consistently improves novel-view accuracy by providing plausible per-frame parameter estimates via the controller.

**Ablation.** We ablate relative contribution of each module in our pipeline through an ablation study on the TANKS AND TEMPLES dataset. Tab. 2 presents the novel view PSNR when individual components are removed from the full pipeline. The results demonstrate that all modules contribute to the full pipeline’s performance, with exposure and vignetting corrections being most critical.

### 5.2. Using Image Metadata

Because our formulation closely mirrors the camera image formation process, it can naturally incorporate image metadata, such as the relative exposure of each frame, whenever available. We demonstrate this capability on the HDR-NeRF [10] and PPISP datasets, both of which use exposure bracketing (*i.e.*, captures with positive and negative exposure compensation) and provide the corresponding metadata.

Since the ADOP-style post-processing also models per-frame exposure offsets explicitly, we initialize them from known exposure values as proposed in ADOP [22]. For our method, we concatenate the exposure metadata to the input of the controller MLP regressor, allowing it to map rendered radiance plus metadata to effective ISP parameters.

Quantitative results in Tab. 3 (PSNR and affine-aligned PSNR) show that supplying calibrated exposure offsets substantially improves novel-view accuracy. Moreover, providing this metadata to the controller yields further gains compared to ADOP, demonstrating our method’s ability to leverage metadata for more accurate novel view appearance prediction.

### 5.3. Runtime Performance

Tab. 4 presents the computational performance of the post-processing methods we evaluated compared to the scene rendering. PPISP (*w/o ctrl.*) and ADOP [22] have a similar and very small computational footprint (3% of the rendering). The controller is adding a substantial overhead due to the required processing of the input image, but our pipeline remains significantly faster (26% vs 36%) compared to BilaRF on an NVIDIA RTX 5090 GPU.

### 5.4. ISP Capacity vs. Training and Novel Views

Next, we investigate how the capacity of the correction module affect the overfitting (difference between the PSNR on training and novel views) and generalization to novel views. The bilateral grids used in BilaRF [28] provide a highly expressive mechanism for modeling image operations [3] extending beyond simple compensation of photometric inconsistencies. In BilaRF [28], this operation is learned independently for each frame, providing a high modeling capacity. In contrast, our PPISP module intentionally has limited capacity to prevent overfitting, but in turn cannot model complex image operations that mix spatial and intensity effects such as localized tone-mapping.

In Tab. 5, we therefore study hybrids of the two approaches. Adding more capacity to per-frame BilaRF [28] with additional per-camera bilateral grids (+PC) does not meaningfully change PSNR on the training views as the model already has sufficient capacity. However, it does slightly improve the generalization as per-camera corrections carry over to novel viewpoints. Increasing our

Table 1. **Novel view synthesis results across five benchmark datasets.** We compare post-processing methods BilaRF [28], ADOP [22], PPISP without controller, and PPISP with controller applied on radiance field reconstruction methods 3DGUT [29] and 3DGS [12, 30]. Metrics with suffix *-CC* denote color-corrected (affine-aligned) versions that factor out global exposure and color differences.

	PSNR $\uparrow$	PSNR-CC $\uparrow$	SSIM $\uparrow$	SSIM-CC $\uparrow$	LPIPS $\downarrow$	LPIPS-CC $\downarrow$
BILARF						
3DGUT [29]	22.60	23.57	0.804	0.794	0.371	0.371
3DGUT + BilaRF [28]	21.41	25.63	0.764	0.806	0.371	0.344
3DGUT + ADOP [22]	22.95	25.73	0.802	0.799	0.376	0.356
3DGUT + PPISP (w/o ctrl.)	24.08	26.16	0.820	0.825	0.346	0.342
3DGUT + PPISP (w/ ctrl.)	24.12	25.92	0.820	0.816	0.349	0.348
3DGS [12, 30]	23.11	24.59	0.799	0.801	0.367	0.365
3DGS + PPISP (w/ ctrl.)	<b>24.86</b>	26.47	<b>0.824</b>	0.828	<b>0.340</b>	0.337
MIP-NeRF 360						
3DGUT [29]	27.74	27.65	<b>0.821</b>	0.813	0.262	0.262
3DGUT + BilaRF [28]	24.97	26.64	0.801	0.807	<b>0.260</b>	0.261
3DGUT + ADOP [22]	26.42	27.75	0.815	0.809	0.271	0.265
3DGUT + PPISP (w/o ctrl.)	27.55	28.02	0.819	0.813	0.264	0.264
3DGUT + PPISP (w/ ctrl.)	<b>28.15</b>	28.06	<b>0.821</b>	0.814	0.264	0.264
3DGS [12, 30]	27.69	27.54	0.818	0.809	0.261	0.261
3DGS + PPISP (w/ ctrl.)	27.98	27.89	0.819	0.811	<b>0.260</b>	0.260
TANKS & TEMPLES						
3DGUT [29]	22.86	23.46	0.790	0.780	0.312	0.311
3DGUT + BilaRF [28]	19.78	23.46	0.770	0.786	0.298	0.289
3DGUT + ADOP [22]	20.28	24.20	0.769	0.783	0.323	0.303
3DGUT + PPISP (w/o ctrl.)	21.52	24.87	0.783	0.793	0.296	0.290
3DGUT + PPISP (w/ ctrl.)	<b>24.62</b>	25.25	<b>0.809</b>	0.805	0.285	0.284
3DGS [12, 30]	23.03	23.66	0.789	0.781	0.303	0.302
3DGS + PPISP (w/ ctrl.)	24.38	25.16	0.807	0.802	<b>0.281</b>	0.279
WAYMO						
3DGUT [29]	25.56	25.21	0.785	0.775	0.397	0.397
3DGUT + BilaRF [28]	21.83	23.66	0.768	0.763	0.397	0.398
3DGUT + ADOP [22]	24.28	25.18	0.781	0.773	0.405	0.400
3DGUT + PPISP (w/o ctrl.)	25.03	25.46	0.786	0.778	<b>0.391</b>	0.391
3DGUT + PPISP (w/ ctrl.)	<b>25.69</b>	25.48	<b>0.787</b>	0.778	<b>0.391</b>	0.392
PPISP-AUTO						
3DGUT [29]	22.05	22.20	0.677	0.658	0.453	0.452
3DGUT + BilaRF [28]	20.81	22.30	0.668	0.660	0.440	0.433
3DGUT + ADOP [22]	19.94	22.52	0.670	0.656	0.462	0.441
3DGUT + PPISP (w/o ctrl.)	21.07	23.14	0.677	0.674	0.438	0.434
3DGUT + PPISP (w/ ctrl.)	<b>22.87</b>	23.21	0.687	0.673	0.434	0.433
3DGS [12, 30]	22.29	22.38	0.679	0.662	0.442	0.441
3DGS + PPISP (w/ ctrl.)	22.85	23.17	<b>0.688</b>	0.675	<b>0.426</b>	0.425

Table 2. Component ablation of PPISP on the Tanks and Temples dataset for novel views (NV). Each row shows performance when removing the specified component.

	NV PSNR $\uparrow$
PPISP (full)	24.62
PPISP - no exposure	23.33
PPISP - no vignetting	24.08
PPISP - no color correction	24.27
PPISP - no CRF	24.36

Table 3. Novel View PSNR across datasets with metadata. Our pipeline is able to leverage metadata (e.g. EXIF) from the sensor as a side data provided to the controller regressor.

metadata	HDR-NeRF [10]		PPISP	
	PSNR $\uparrow$	PSNR-CC $\uparrow$	PSNR $\uparrow$	PSNR-CC $\uparrow$
3DGUT [29]	17.81	27.37	12.44	18.59
[29] + BilaRF [28]	15.40	26.95	13.39	20.89
[29] + ADOP [22]	15.49	24.14	13.36	17.34
	31.27	36.10	20.44	21.60
[29] + PPISP	17.86	27.78	14.69	21.19
	<b>34.30</b>	37.10	<b>21.69</b>	21.94

Table 4. Rendering times (ms) on NVIDIA RTX 5090 for the MipNeRF 360 [2] dataset.

	Time (ms) $\downarrow$	% overhead $\downarrow$
3DGUT [29]	3.24	—
BilaRF [28]	1.17	36%
ADOP	0.10	3%
PPISP (w/o ctrl.)	0.10	3%
PPISP (w/ ctrl.)	0.84	26%

Table 5. Average PSNR on the Tanks and Temples dataset comparing training views (TV) and novel views (NV) for ISP modules with varying capacity. The limited capacity of our proposed pipeline reduces overfitting and leads to better generalization.

	TV PSNR $\uparrow$	NV PSNR $\uparrow$
BilaRF + PC	26.83	21.80
PPISP + BilaRF [28]	26.66	23.52
BilaRF [28]	<b>26.87</b>	19.78
ADOP [22]	26.08	20.28
PPISP	25.85	<b>24.62</b>

method’s capacity by adding per-frame bilateral grids boosts PSNR on the training views, but noticeably degrades performance on novel views due to overfitting. Overall, our formulation achieves a favorable balance between capacity and generalization to unseen views.

## 6. Conclusion and Limitations

Accurately reconstructing the radiance field of a scene requires accounting for variations in the camera imaging pipeline across the input frames. Ignoring these variations introduces strong biases, leading to spurious color shifts and geometric artifacts. In this work, we introduced a differentiable post-processing pipeline whose design permits to simulate the imaging process while remaining highly constrained to prevent reconstruction bias. We further proposed a controller that improves generalization to novel views by predicting per-frame imaging parameters directly from the rendered radiance.

**Limitations.** Our method shows superior generalization to novel views (Tab. 1), but it sometimes struggles to match the baselines on the training-views (Tab. 5). This can be partially accredited to overfitting, but our formulation also ignores some important optical effects such as localized tone-mapping commonly found in modern phone cameras; lens flares, which are prominent in night scenes; and similar spatially-adaptive effects. While the proposed controller enables generalization to novel views, its ability to infer exposure and color-correction parameters from rendered radiance depends on the existence of meaningful correlations in

the data. When such correlations are absent, for example when the physical camera controls (e.g., shutter, aperture, ISO) are manually overridden, the controller must rely on extra metadata to predict correct values.

## 7. Acknowledgements

We thank our colleagues Qi Wu, Janick Martinez Esturo, András Bódás-Szomorú, and Nick Schneider for their suggestions, feedback, and valuable discussions.

## References

- [1] Hadi Alzayer, Philipp Henzler, Jonathan T. Barron, Jia-Bin Huang, Pratul P. Srinivasan, and Dor Verbin. Generative multiview relighting for 3d reconstruction under extreme illumination variation. In *Proceedings of the Computer Vision and Pattern Recognition Conference (CVPR)*, pages 10933–10942, 2025. [2](#)
- [2] Jonathan T. Barron, Ben Mildenhall, Dor Verbin, Pratul P. Srinivasan, and Peter Hedman. Mip-nerf 360: Unbounded anti-aliased neural radiance fields. In *CVPR*, 2022. [2, 7, 9, 6](#)
- [3] Jiawen Chen, Andrew Adams, Neal Wadhwa, and Samuel W Hasinoff. Bilateral guided upsampling. *ACM Transactions on Graphics (TOG)*, 35(6):1–8, 2016. [7](#)
- [4] Daniel DeTone, Tomasz Malisiewicz, and Andrew Rabinovich. Deep image homography estimation, 2016. Preprint. [4](#)
- [5] Daniel Duckworth, Peter Hedman, Christian Reiser, Peter Zhizhin, Jean-François Thibert, Mario Lučić, Richard Szeliski, and Jonathan T. Barron. Smerf: Streamable memory efficient radiance fields for real-time large-scene exploration, 2023. [2](#)
- [6] Graham Finlayson, Han Gong, and Robert B. Fisher. Color homography: theory and applications. *IEEE TPAMI*, 41(1):20–33, 2017. [4](#)
- [7] Daniel B Goldman. Vignette and exposure calibration and compensation. *IEEE transactions on pattern analysis and machine intelligence*, 32(12):2276–2288, 2010. [4](#)
- [8] Michael D. Grossberg and Shree K. Nayar. Determining the camera response from images: What is knowable? *IEEE TPAMI*, 25(11):1455–1467, 2003. [4, 2](#)
- [9] Michael D. Grossberg and Shree K. Nayar. Modeling the space of camera response functions. *IEEE TPAMI*, 26(10):1272–1282, 2004. [4](#)
- [10] Xin Huang, Qi Zhang, Ying Feng, Hongdong Li, Xuan Wang, and Qing Wang. Hdr-nerf: High dynamic range neural radiance fields. In *CVPR*, pages 18398–18408, 2022. [7, 8, 2, 5, 6](#)
- [11] Xin Huang, Qi Zhang, Ying Feng, Hongdong Li, and Qing Wang. Ltm-nerf: Embedding 3d local tone mapping in hdr neural radiance field. *IEEE TPAMI*, 2024. [2](#)
- [12] Bernhard Kerbl, Georgios Kopanas, Thomas Leimkühler, and George Drettakis. 3d gaussian splatting for real-time radiance field rendering. *ACM Transactions on Graphics*, 42(4), 2023. [6, 7, 8](#)

[13] Agnan Kessy, Alex Lewin, and Korbinian Strimmer. Optimal whitening and decorrelation. *The American Statistician*, 72(4):309–314, 2018. 4

[14] Arno Knapitsch, Jaesik Park, Qian-Yi Zhou, and Vladlen Koltun. Tanks and temples: Benchmarking large-scale scene reconstruction. *ACM Transactions on Graphics*, 36(4), 2017. 7, 5, 6

[15] Ricardo Martin-Brualla, Noha Radwan, Mehdi S. M. Sajjadi, Jonathan T. Barron, Alexey Dosovitskiy, and Daniel Duckworth. Nerf in the wild: Neural radiance fields for unconstrained photo collections. In *CVPR*, pages 7210–7219, 2021. 1, 2

[16] Ben Mildenhall, Peter Hedman, Ricardo Martin-Brualla, Pratul P. Srinivasan, and Jonathan T. Barron. NeRF in the dark: High dynamic range view synthesis from noisy raw images. In *CVPR*, 2022. 2, 6

[17] Michael Niemeyer, Fabian Manhardt, Marie-Julie Rakotosaona, Michael Oechsle, Christina Tsalicoglou, Keisuke Tateno, Jonathan T. Barron, and Federico Tombari. Learning neural exposure fields for view synthesis. In *NeurIPS*, 2025. to appear. 2

[18] Emmanuel Onzon, Fahim Mannan, and Felix Heide. Neural auto-exposure for high-dynamic range object detection. In *Proceedings of the IEEE/CVF Conference on Computer Vision and Pattern Recognition*, 2021. 3

[19] Linfei Pan, Daniel Barath, Marc Pollefeys, and Johannes Lutz Schönberger. Global Structure-from-Motion Revisited. In *ECCV*, 2024. 6

[20] Keunhong Park, Philipp Henzler, Ben Mildenhall, Jonathan T. Barron, and Ricardo Martin-Brualla. Camp: Camera preconditioning for neural radiance fields. *ACM TOG*, 42(6):1–11, 2023. 4

[21] Konstantinos Rematas, Andrew Liu, Pratul P. Srinivasan, Jonathan T. Barron, Andrea Tagliasacchi, Tom Funkhouser, and Vittorio Ferrari. Urban radiance fields. *CVPR*, 2022. 1, 2

[22] Darius Rückert, Linus Franke, and Marc Stamminger. Adop: Approximate differentiable one-pixel point rendering. *ACM TOG*, 41(4):99:1–99:14, 2022. 2, 6, 7, 8, 9, 1, 3, 4, 5

[23] Johannes Lutz Schönberger and Jan-Michael Frahm. Structure-from-motion revisited. In *CVPR*, 2016. 6

[24] Jisu Shin, Richard Shaw, Seunghyun Shin, ZhenSong Zhang, Hae-Gon Jeon, and Eduardo Perez-Pellitero. Chroma: Consistent harmonization of multi-view appearance via bilateral grid prediction, 2025. Preprint. 2

[25] Pei Sun, Henrik Kretzschmar, Xerxes Dotiwalla, Aurelien Chouard, Vijaysai Patnaik, Paul Tsui, James Guo, Yin Zhou, Yuning Chai, Benjamin Caine, Vijay Vasudevan, Wei Han, Jiquan Ngiam, Hang Zhao, Aleksei Timofeev, Scott Ettinger, Maxim Krivokon, Amy Gao, Aditya Joshi, Yu Zhang, Jonathon Shlens, Zhifeng Chen, and Dragomir Anguelov. Scalability in perception for autonomous driving: Waymo open dataset. In *CVPR*, 2020. 7, 5, 6

[26] Justin Tomasi, Brandon Wagstaff, Steven L Waslander, and Jonathan Kelly. Learned camera gain and exposure control for improved visual feature detection and matching. *IEEE Robotics and Automation Letters*, 6(2):2028–2035, 2021. 3

[27] Alex Trevithick, Roni Paiss, Philipp Henzler, Dor Verbin, Rundi Wu, Hadi Alzayer, Ruiqi Gao, Ben Poole, Jonathan T. Barron, Aleksander Holynski, Ravi Ramamoorthi, and Pratul P. Srinivasan. Simvs: Simulating world inconsistencies for robust view synthesis. *arXiv*, 2024. 2

[28] Yuehao Wang, Chaoyi Wang, Bingchen Gong, and Tianfan Xue. Bilateral guided radiance field processing. *ACM TOG*, 43(4):148:1–148:13, 2024. 1, 2, 6, 7, 8, 9, 3, 5

[29] Qi Wu, Janick Martinez Esturo, Ashkan Mirzaei, Nicolas Moenne-Loccoz, and Zan Gojcic. 3dgut: Enabling distorted cameras and secondary rays in gaussian splatting. In *CVPR*, 2025. 6, 8, 9, 3

[30] Vickie Ye, Ruilong Li, Justin Kerr, Matias Turkulainen, Brent Yi, Zhuoyang Pan, Otto Seiskari, Jianbo Ye, Jeffrey Hu, Matthew Tancik, and Angjoo Kanazawa. gsplat: An open-source library for gaussian splatting. *Journal of Machine Learning Research*, 26(34):1–17, 2025. 6, 7, 8

[31] Dongbin Zhang, Chuming Wang, Weitao Wang, Peihao Li, Minghan Qin, and Haoqian Wang. Gaussian in the wild: 3d gaussian splatting for unconstrained image collections. In *European Conference on Computer Vision*, pages 341–359. Springer, 2024. 2

# PPISP: Physically-Plausible Compensation and Control of Photometric Variations in Radiance Field Reconstruction

## Supplementary Material

This supplementary material provides additional experiments, method details, and implementation specifications to complement the main paper.

Sec. A presents extended experimental results, including a detailed comparisons with ADOP’s image formation model [22] and additional experiments on components (camera calibration and exposure identifiability).

Sec. B provides further method details, *i.e.*, mathematical derivations of our color correction formulation and specifications of our per-frame controller architecture.

Sec. C details optimization settings, regularization weights, learning rate schedules, and dataset specifications used throughout our experiments.

Finally, Sec. D discusses interactive manual control capabilities of our method.

## A. Additional Experiments

To complete the main paper experiments, we provide further qualitative results in Fig. 5 and present the detail of the novel-view PSNR for every scene in Tab. 6.

### A.1. Detailed Comparison with ADOP [22]

In the related work (Sec. 2), we mention that ADOP [22] implements a similar image formation model as ours. We deviate in the color correction and CRF. Here, we provide a detailed comparison, expanding on the main results in Sec. 5.

**White balance and exposure decoupling.** In Sec. 4.3, we claim that our color correction method, which operates on 2D chromaticities instead of 3D color and normalizes the intensity post-transformation, decouples the white balance from the exposure correction. We evaluate this by computing the Pearson correlation coefficient (PCC) between the estimated exposure offset and the white point offset,  $\Delta c_W$ , which controls the white balance and compare our method against ADOP’s which uses per-channel white-point gains.

The PCC is defined as:

$$r_{X,Y} = \frac{\text{cov}(X, Y)}{\sigma_X \sigma_Y} \quad (23)$$

where  $r_{X,Y}$  is the Pearson correlation coefficient between variables  $X$  and  $Y$ ,  $\text{cov}(X, Y)$  is the covariance between  $X$  and  $Y$ , and  $\sigma_X$  and  $\sigma_Y$  are the standard deviations of  $X$  and  $Y$ , respectively. A PCC near 1 indicates strong linear correlation, and a PCC near 0 indicates weak or no correlation.

A representative result is shown in Fig. 6. We find that the PCC numbers for our method are substantially lower as

compared to ADOP’s method on all sequences, indicating an improved decoupling of white balance and exposure correction.

Figure 7 further highlights the importance of decoupling color and exposure corrections: When exposure and color are coupled, the CRF will also be entangled in order to compensate for the value-dependent color shift. That, in turn, hinders the controllability of both aspects since neither can be changed without also affecting the other.

**CRF stability in challenging sequences.** In Sec. 4.4, we provide a formulation for the camera response function that is constrained to be monotonically increasing and smooth by design. This ensures that the optimization remains stable. In some sequences, particularly when large photometric variations were present, we found that this offers an improvement over ADOP’s [22] CRF formulation, which uses 25 discrete nodes which are interpolated linearly and requires a smoothness loss. A degenerate case of ADOP’s CRF is illustrated in Fig. 7 (third row), where the learned green and red channels of the CRF are split into lower and upper sections with a reversal. This violates the assumption that the CRF is monotonically increasing. While the post-processed image still remains close in brightness and color to the actual scene due to corrections being self-consistent, it falls apart with strong color artifacts when applying a controlled exposure offset.

### A.2. Online Camera Calibration

Since certain parts of the PPISP pipeline, namely the vignetting (Sec. 4.2) and CRF (Sec. 4.4), are shared across all frames of a camera, the process of jointly optimizing them with the radiance field reconstruction can be understood as an online camera calibration. We compared the recovered per-camera parameters across multiple sequences qualitatively in Fig. 8, where multiple plots are overlaid. Same color implies same dataset. The close overlap of the curves from the same datasets and the distinct shapes between datasets indicate that our method can robustly extract these calibrations. It also suggests that the camera-specific curves are disentangled from scene radiance and other corrective effects, otherwise we would expect an ambiguous mixing of them.

### A.3. Identifiability of Exposure Offsets

In Sec. 5.2, we tested the effectiveness of using image exposure metadata to guide the image formation process. Here, we consider the inverse problem of identifying calibrated



Figure 5. Qualitative comparison of novel view synthesis, additional examples. Row labels indicate datasets and sequences (in italics). Column labels indicate methods.

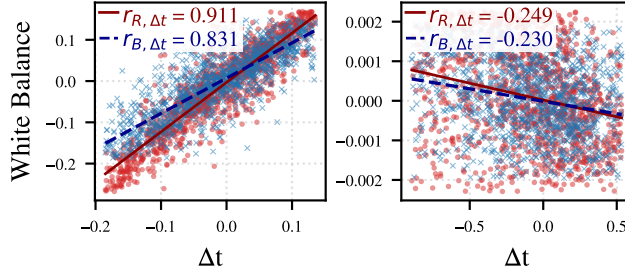


Figure 6. Correlation between optimized exposure offset and white balancing variables in SMERF’s [5] *alameda* sequence. Left: ADOP’s [22] red and blue channel scaling. Right: The offsets of the white point of our homography-based correction. The Pearson correlation coefficient for each component is inset.

exposure offsets. In this experiment, per-frame exposure offsets are freely optimized and compared against the relative exposure metadata present in the HDR-NeRF [10] and PPISP datasets.

According to Grossberg and Nayar [8], there is an “exponential ambiguity”, which states that transforming both the inverse of the CRF and the radiance by some power produces exactly the same image intensities. Since our exposure offsets are parameterized in log-space, applying a power to the radiance corresponds to a scaling in parameter space. Thus, for this experiment, we apply an optimal affine transform on the recovered exposure offsets and compute the error on the transformed data.

As illustrated in Fig. 9 for a representative sequence, calibrated exposure metadata is matched closely.

## B. Additional Method Details

### B.1. Color Correction

In Sec. 4.3, we propose a color correction method based on a  $3 \times 3$  homography matrix  $\mathbf{H}$ , applied on RG chromaticities and intensity, followed by an intensity normalization. For the parameterization of  $\mathbf{H}$ , we show a construction from chromaticity offsets  $\Delta \mathbf{c}_k$  that control the mapping from source to target chromaticities. In this section, we provide a more detailed derivation.

Furthermore, we detail the preconditioning we apply to the chromaticity offsets  $\Delta \mathbf{c}_k$ .

**Derivation and equivalence to direct linear transformation.** We derive the construction of  $\mathbf{H}$  in detail and show that the resulting matrix is equivalent to the standard method for constructing homography matrices from source-target pairs, the direct linear transformation (DLT).

In Sec. 4.3, we define source and target chromaticity vector pairs  $\mathbf{c}_{\{s,t\},\{R,G,B,W\}}$ . The homogeneous lifts of these vectors are denoted with a tilde,  $\tilde{\mathbf{c}}_{\{s,t\},\{R,G,B,W\}}$ . The  $\mathbf{S}$  and  $\mathbf{T}$  matrices are built by stacking the lifted source and target red, green, and blue chromaticity vectors, respectively. We note that  $\mathbf{S}$  is constant and has an inverse  $\mathbf{S}^{-1}$ .

**Reduction using three correspondences.** By definition, a homography is a colinear transformation (collineation), *i.e.*, transformed vectors are identical to the original ones up to scale:  $\mathbf{H} \tilde{\mathbf{c}}_{s,i} \sim \tilde{\mathbf{c}}_{t,i}$  for  $i \in \{R, G, B\}$ . Using the stacked matrices  $\mathbf{S}$  and  $\mathbf{T}$ , it follows that there exist nonzero

Table 6. **Per-scene novel view PSNR comparison.** We compare post-processing methods applied on top of 3DGUT reconstruction across all sequences. Higher is better ( $\uparrow$ ).

Dataset	Scene	3DGUT [29]	+ BilaRF [28]	+ ADOP [22]	+ PPISP (w/o ctrl.)	+ PPISP (w/ ctrl.)
BILARF						
building		24.85	22.81	25.30	26.36	<b>26.46</b>
chineseearch		18.34	20.44	21.27	<b>22.13</b>	21.62
lionpavilion		24.16	24.11	22.89	<b>25.06</b>	24.76
nightimepond		27.11	21.54	25.07	27.68	<b>28.16</b>
pondbike		25.28	21.17	24.96	<b>26.33</b>	26.04
statue		22.40	21.01	<b>22.84</b>	<b>22.84</b>	22.26
strat		16.06	18.76	18.34	18.17	<b>19.55</b>
MIP-NERF 360						
bicycle		25.28	24.26	24.54	24.95	<b>25.72</b>
bonsai		32.52	28.57	30.33	32.10	<b>33.02</b>
counter		29.36	26.30	27.58	28.89	<b>29.50</b>
flowers		21.80	20.10	21.54	21.76	<b>21.95</b>
garden		26.85	24.06	26.10	27.14	<b>27.31</b>
kitchen		31.86	27.50	28.08	30.51	<b>32.14</b>
room		32.11	29.53	30.76	32.95	<b>32.84</b>
stump		26.90	24.90	26.59	27.03	<b>27.28</b>
treehill		22.97	19.46	22.25	22.59	<b>23.55</b>
TANKS AND TEMPLES						
caterpillar		22.61	19.19	18.15	19.74	<b>25.18</b>
ignatius		22.03	20.01	20.47	20.77	<b>24.04</b>
train		22.06	19.04	18.95	20.17	<b>23.74</b>
truck		24.72	20.88	23.56	25.38	<b>25.51</b>
WAYMO						
10275144660749673822_5755_561_5775_561		24.73	20.59	23.68	24.30	<b>25.17</b>
1265122081809781363_2879_530_2899_530		<b>28.39</b>	24.47	26.30	27.50	28.31
15959580576639476066_5087_580_5107_580		27.52	24.06	26.54	27.04	<b>27.77</b>
16470190748368943792_4369_490_4389_490		23.82	20.17	22.09	23.69	<b>24.21</b>
16608525782988721413_100_000_120_000		<b>23.29</b>	19.86	22.62	22.91	23.27
16646360389507147817_3320_000_3340_000		<b>26.65</b>	23.71	24.84	25.86	26.48
17244566492658384963_2540_000_2560_000		27.25	22.19	26.00	26.31	<b>27.39</b>
1999080374382764042_7094_100_7114_100		24.10	20.85	23.18	23.65	<b>24.34</b>
744006317457557752_2080_000_2100_000		24.26	20.53	23.31	24.05	<b>24.30</b>
PPISP-AUTO						
huerstholz_auto		19.23	18.76	18.88	19.24	<b>19.81</b>
struktur28_auto		24.21	22.80	21.97	22.25	<b>25.28</b>
toro_auto		22.24	20.56	18.44	20.20	<b>23.01</b>
valiant_auto		22.51	21.14	20.47	22.58	<b>23.39</b>

$\mathbf{k} = (k_R, k_G, k_B)^\top$  such that

$$\mathbf{H} \mathbf{S} = \mathbf{T} \operatorname{diag}(\mathbf{k}) \implies \mathbf{H}(\mathbf{k}) = \mathbf{T} \operatorname{diag}(\mathbf{k}) \mathbf{S}^{-1}. \quad (24)$$

Thus, the homography is reduced to three column scales up to a common factor.

**Fourth correspondence via colinearity.** To find  $\mathbf{k}$ , we write the source white point as  $\tilde{\mathbf{c}}_{s,W} = \mathbf{S} \mathbf{b}$  with barycentric  $\mathbf{b} = (\frac{1}{3}, \frac{1}{3}, \frac{1}{3})^\top$ .

We require  $\mathbf{H} \tilde{\mathbf{c}}_{s,W} \sim \tilde{\mathbf{c}}_{t,W}$ . Another way to express this colinearity constraint is  $\tilde{\mathbf{c}}_{t,W} \times (\mathbf{T} \operatorname{diag}(\mathbf{b}) \mathbf{k}) = \mathbf{0}$ . Using the skew-symmetric matrix  $[\cdot]_\times$  with  $[\mathbf{x}]_\times \mathbf{y} = \mathbf{x} \times \mathbf{y}$ ,

this yields the homogeneous linear system

$$[\tilde{\mathbf{c}}_{t,W}]_\times \mathbf{T} \operatorname{diag}(\mathbf{b}) \mathbf{k} = \mathbf{0}.$$

For the white point,  $\operatorname{diag}(\mathbf{b}) \propto \mathbf{I}$ , so the constraint reduces to the  $3 \times 3$  system  $\mathbf{M} \mathbf{k} = \mathbf{0}$  with  $\mathbf{M} = [\tilde{\mathbf{c}}_{t,W}]_\times \mathbf{T}$ . Generically  $\operatorname{rank}(\mathbf{M}) = 2$ , so the right nullspace is 1D and determines  $\mathbf{k}$  up to scale. A practical closed form is to take any cross of two independent rows  $\mathbf{r}_i, \mathbf{r}_j$  of  $\mathbf{M}$ , i.e.:  $\mathbf{k} \propto \mathbf{r}_i \times \mathbf{r}_j$ . Substituting  $\mathbf{k}$  into  $\mathbf{H}(\mathbf{k})$  and normalizing by an arbitrary scalar (e.g., set  $[\mathbf{H}]_{3,3} = 1$ ) gives the desired homography.

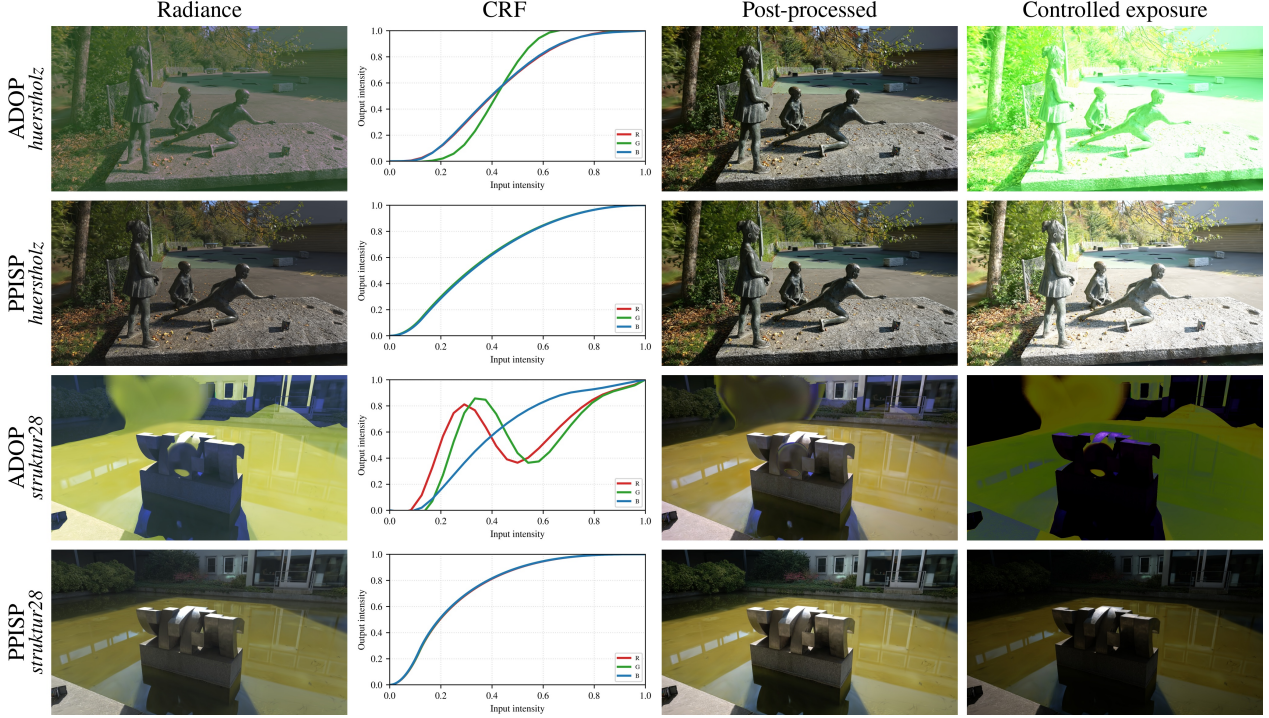


Figure 7. Comparison of ADOP [22]-style post-processing including exposure control against our method. Row labels indicate the post-processing method and the sequence name (in italics). The CRF for ADOP’s formulation compensates for the color artifacts baked into the radiance field only at a specific exposure value. But when controlling exposure for novel views, color artifacts are exacerbated. In contrast, both our method’s radiance field and output remain neutral since all corrections are decoupled.

**Equivalence to the 4-point DLT.** The classical DLT stacks the four constraints into  $\mathbf{A} \mathbf{h} = \mathbf{0}$  for the 9-vector  $\mathbf{h}$  (up to scale), and solves for the 1D right-nullspace of  $\mathbf{A}$ . Our construction enforces the same constraints factorized through the invertible  $\mathbf{S}$ : three correspondences reduce to the column scales  $\mathbf{k}$ , and the fourth yields  $\mathbf{M} \mathbf{k} = \mathbf{0}$ . Under non-degenerate configurations (*i.e.*, the columns of  $\mathbf{T}$  are not colinear and  $\text{rank}(\mathbf{M}) = 2$ ), both methods recover the same  $\mathbf{H}$  up to an overall scalar.

**Degeneracies and identity case.** If  $\text{rank}(\mathbf{T}) < 2$  or  $\text{rank}(\mathbf{M}) < 2$ ,  $\mathbf{k}$  is ill-defined, mirroring DLT degeneracies. When targets equal sources,  $\mathbf{T} = \mathbf{S}$ ,  $\tilde{\mathbf{c}}_{t,W} = \tilde{\mathbf{c}}_{s,W}$ , and  $\mathbf{k} \propto (1, 1, 1)$ , yielding  $\mathbf{H}$  proportional to the identity after normalization.

**Preconditioning of the chromaticity offsets.** Our color correction method involves a conversion from RGB color to RGI (red-green chromaticity and intensity) and back, with  $I = R + G + B$  and  $B = I - R - G$  in terms of components. In our optimization setting, this correlates the gradients of the individual chromaticity offsets  $\{\Delta \mathbf{c}_i\}$  with the blue channel. In addition to that, the output image is generally more sensitive to changes in the white point than an

offset in the RGB primaries.

In order to whiten the color correction and decorrelate the individual components, we apply ZCA preconditioning with proxy Jacobians following [13, 20]. We precondition the 8-dimensional vector of chromaticity offsets  $\{\Delta \mathbf{c}_i\}_{i \in \{R, G, B, W\}}$ . We use a block decomposition into four  $2 \times 2$  blocks (one per control point) in place of the full  $8 \times 8$  transform.

## B.2. Controller Architecture

The overall architecture of the per-frame ISP controller is given in Sec. 4.5. Here, we provide the complete architectural specifications.

**Input and output.** The controller takes as input the rendered scene radiance  $\mathbf{L} \in \mathbb{R}^{H \times W \times 3}$ . Extra inputs, such as image metadata, are input at the beginning of the parameter regression stage.

The controller outputs 9 parameters: an exposure offset  $\Delta t \in \mathbb{R}$  and eight color correction offsets  $\{\Delta \mathbf{c}_i\}_{i \in \{R, G, B, W\}}$ .

**Feature extraction stage.** The feature extractor processes the input radiance using a sequence of 1x1 convolutions and pooling operations.

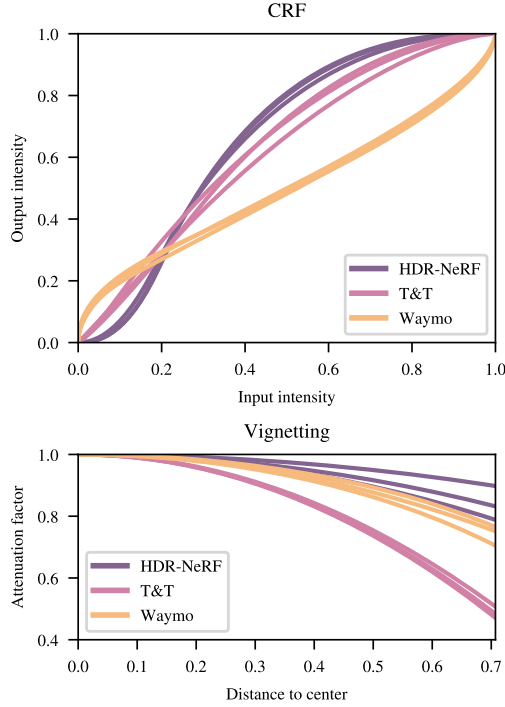


Figure 8. Recovered camera-specific parameters across datasets. Top: The calibrated CRF of three sequences of each of the HDR-NeRF [10], Tanks and Temples [14], and Waymo Open Drive [25] dataset are overlaid. Bottom: For the same sequences and datasets, the vignetting falloff curves are compared.

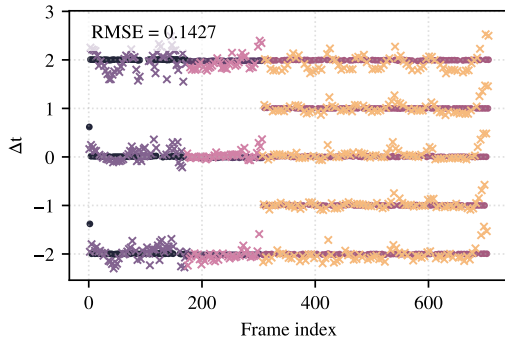


Figure 9. Optimized exposure parameters per frame and given exposure metadata for the *huerstholz* sequence in the PPISP dataset. Colors indicate individual cameras.

First, a  $1 \times 1$  convolution maps the 3-channel input to 16 feature channels. This is followed by max pooling with a factor of 3 in each spatial dimension, reducing the resolution to  $H/3 \times W/3$ . A ReLU activation is then applied. Next, a second  $1 \times 1$  convolution expands the features to 32 channels, followed by ReLU. A third  $1 \times 1$  convolution produces 64 feature channels, yielding a feature map  $\mathbf{F} \in \mathbb{R}^{H/3 \times W/3 \times 64}$ .

Then, spatial aggregation is performed. An adaptive

average pooling operation reduces the spatial dimensions to a  $5 \times 5$  grid, producing a coarse feature representation  $\mathbf{F}_{\text{pool}} \in \mathbb{R}^{5 \times 5 \times 64}$ . This grid captures multi-scale spatial statistics of the scene while maintaining spatial locality, analogous to metering zones in conventional cameras.

**Parameter regression stage.** The pooled features are flattened into a 1600-dimensional vector ( $5 \times 5 \times 64$ ). If available, image metadata may be concatenated at this stage. This is input into an MLP with three hidden layers, each containing 128 neurons with ReLU activations. The output consists of two parallel linear heads: one producing the exposure offset and the other producing the 8 color correction parameters.

### C. Additional Experiment Details

We provide optimization hyperparameters, regularization weights, and dataset specifications used throughout our experiments.

#### C.1. Optimization settings

**Regularization weights.** In Sec. 4.6, we specify the regularizer terms that break brightness and color ambiguities and ensure physically-plausible vignetting. In Tab. 7, we detail the numerical values used for each  $\lambda$  term.

Table 7. Regularization coefficients.

Term	$\lambda$
$\lambda_b$	1.0
$\lambda_c$	1.0
$\lambda_{\text{var}}$	0.1
$\lambda_v$	0.01

**Optimizer, learning rates, and schedules.** For all post-processing modules including BilaRF [28], ADOP’s formulation [22], and our method, we use the Adam optimizer. We use the following learning rate scheduling with an initial delay (zero learning rate), linear warmup, and exponential decay.

$$lr(s) = \begin{cases} 0, & s < s_d, \\ lr_0 \left[ f_s + (1 - f_s) \frac{s - s_d}{s_w} \right], & s_d \leq s < s_d + s_w, \\ lr_0 \left( f_f^{1/s_{\max}} \right)^{s - s_d - s_w}, & s \geq s_d + s_w. \end{cases} \quad (25)$$

Where:

- $lr_0$  — base learning rate.
- $s$  — current training step.
- $s_d$  — delay steps (learning rate held at zero).
- $s_w$  — warmup steps (linear ramp from  $f_s lr_0$  to  $lr_0$ ).
- $s_{\max}$  — number of decay steps.

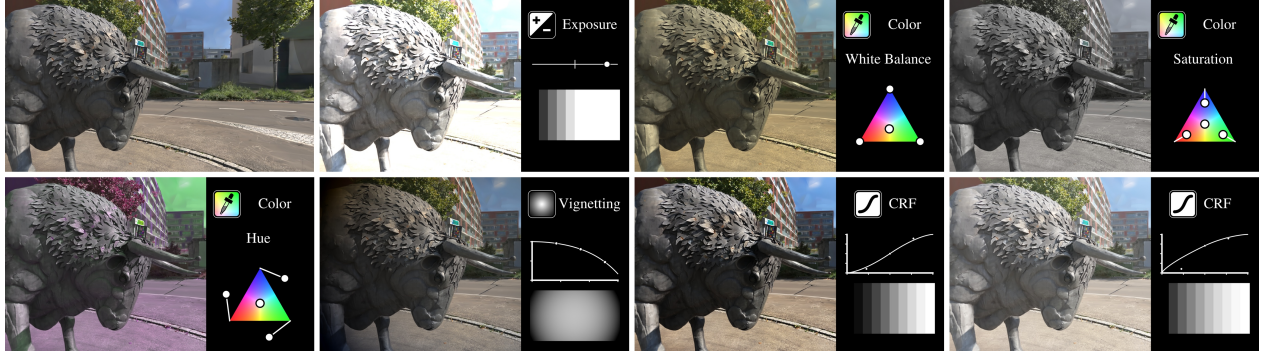


Figure 10. Our low-parametric formulation of the different image processing steps enables manual editing. Top left shows the input image. Other images have details overlaid, such as the primary effect being applied and an abstract visualization. In the color correction examples, the white dots correspond to the four target chromaticities  $\mathbf{c}_{t,\{R,G,B,W\}}$ , which can be intuitively manipulated.

- $f_s$  — start factor for warmup (e.g., 0.01).
- $f_f$  — final factor reached after decay (e.g., 0.01).

Tab. 8 details the values used during experiments.

Table 8. Learning rate scheduler hyperparameters.

Term	Value
$lr_0$	0.002
$s_d$	0
$s_w$	500
$f_s$	0.01
$s_{\max}$	30000
$f_f$	0.01

In Sec. 5.4, we experiment with combined post-processing methods. In these cases, the BilaRF module as combined with PPISP and per-camera bilateral grids use  $s_d = 5000$  and  $s_w = 1000$  with otherwise the same hyperparameters as in Tab. 8.

## C.2. Datasets

In Sec. 5, we outline the datasets used for experiments. In this section, we define the datasets in more detail.

**Specific choice of sequences.** We chose the following sequences from each dataset:

- Mip-NeRF 360 [2]: All nine sequences,
- Tanks and Temples [14]: Four sequences, namely *train*, *truck*, *caterpillar*, and *ignatius*,
- BilaRF [28]: All seven sequences,
- HDR-NeRF [10]: All four real-camera sequences,
- Waymo Open Dataset [25]: Nine mostly static sequences, explicitly listed in Tab. 9; All five cameras used.

**PPISP dataset details.** As stated in Sec. 5, we captured our own dataset using three cameras, including two modern

Table 9. Waymo Open Dataset [25] sequence names.

Sequence Name
74400631745755752_2080_000_2100_000
126512208180978136_2879_530_2899_530
199908037438276404_7094_100_7114_100
102751446607496738_5755_561_5775_561
159595805766394760_5087_580_5107_580
164701907483689437_4369_490_4389_490
166085257829887214_100_000_120_000
166463603895071478_3320_000_3340_000
172445664926583849_2540_000_2560_000

mirrorless and a smartphone camera. We provide further context here.

For all cameras and scenes, we used exposure bracketing of  $\pm 2$  EV to capture HDR data. The aperture and focus were set manually and remained fixed. Image stabilization was disabled. Each scene was captured in raw format. The raw photos were developed with NX Studio and OM Workspace for the Nikon and OM System photos, and Adobe Lightroom Classic for the iPhone photos, respectively. A color calibration target placed in the scene was used to white balance.

For each scene, we additionally picked certain exposures out of the brackets and re-developed them with normalized, automatic exposure compensation and white balancing, creating a more challenging setting for the controller module. We denote this derived dataset *PPISP-auto*.

**Pre-processing.** For all datasets including our own, where camera poses or sparse point clouds were not originally available, we processed them through COLMAP [23] and GLOMAP [19] to produce the necessary inputs for the radiance field reconstruction.

We used downsampled versions of the original camera images so that the maximum effective side length of each input image did not exceed 2000 pixels. *E.g.*, for Mip-NeRF 360’s [2] *garden* sequence, we used  $4\times$  downsampling, and for *bonsai*, we used  $2\times$ .

We used a seven to one split of test views to validation views for evaluation throughout.

## D. Manual Control

Our parametric ISP formulation enables intuitive manual editing and artistic control. Fig. 10 demonstrates various edits applied to a reconstructed scene, including adjustments to exposure, white balance, vignetting, and camera response. The low-dimensional and disentangled representation ensures meaningful and predictable edits, facilitating interactive workflows for applications such as artistic rendering, temporal consistency enforcement, or selective photometric matching.